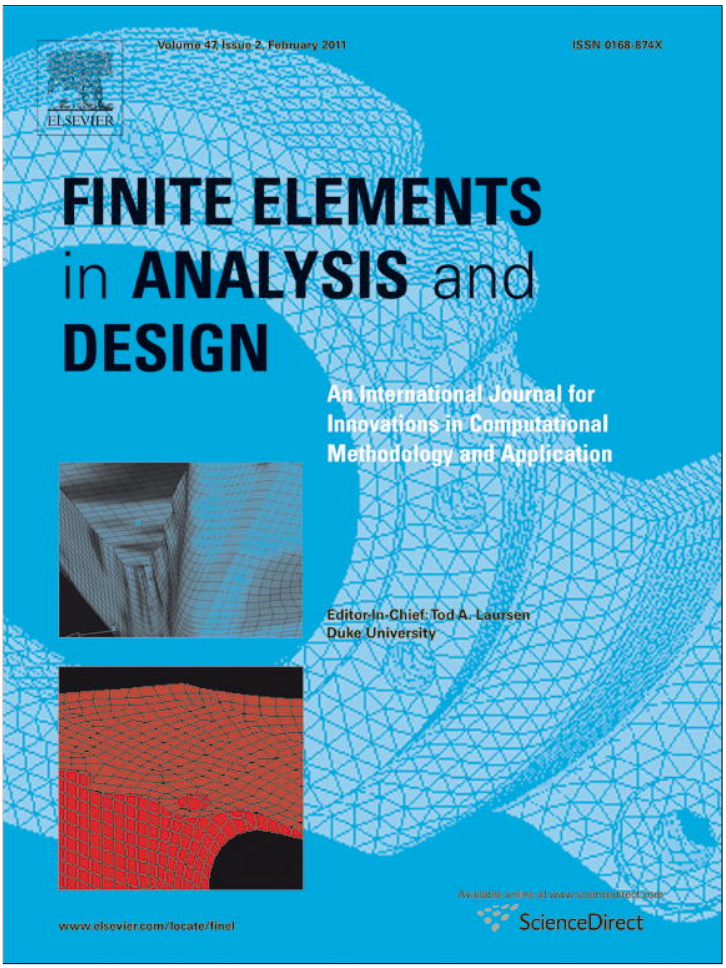

Finite Elements in Analysis and Design 47 (2011) 166–174

Contents lists available at ScienceDirect

Finite Elements in Analysis and Design

journal homepage: www.elsevier.com/locate/finel

An improved, fully symmetric, finite-strain phenomenological constitutive model for shape memory alloys

J. Arghavani [a,*,1], F. Auricchio [b,c,d], R. Naghdabadi [a,e], A. Reali [b,d]

[a] Department of Mechanical Engineering, Sharif University of Technology, 11155-9567 Tehran, Iran
[b] Dipartimento di Meccanica Strutturale, Università degli Studi di Pavia, Italy
[c] Center for Advanced Numerical Simulation (CeSNA), IUSS, Pavia, Italy
[d] European Centre for Training and Research in Earthquake Engineering (EUCENTRE), Pavia, Italy
[e] Institute for Nano-Science and Technology, Sharif University of Technology, 11155-9567 Tehran, Iran

ARTICLE INFO

Article history:
Received 31 May 2010
Accepted 6 September 2010
Available online 28 September 2010

Keywords:
Shape memory alloys
Finite strain
Solution algorithm
Finite element
Exponential mapping
UMAT

ABSTRACT

The ever increasing number of shape memory alloy applications has motivated the development of appropriate constitutive models taking into account large rotations and moderate or finite strains. Up to now proposed finite-strain constitutive models usually contain an asymmetric tensor in the definition of the limit (yield) function. To this end, in the present work, we propose an improved alternative constitutive model in which all quantities are symmetric. To conserve the volume during inelastic deformation, an exponential mapping is used to arrive at the time-discrete form of the evolution equation. Such a symmetric model simplifies the constitutive relations and as a result of less nonlinearity in the equations to be solved, numerical efficiency increases. Implementing the proposed constitutive model within a user-defined subroutine UMAT in the nonlinear finite element software ABAQUS/Standard, we solve different boundary value problems. Comparing the solution CPU times for symmetric and asymmetric cases, we show the effectiveness of the proposed constitutive model as well as of the solution algorithm. The presented procedure can also be used for other finite-strain constitutive models in plasticity and shape memory alloy constitutive modeling.

1. Introduction

Shape memory alloys (SMAs) are unique materials with the ability to undergo large deformations regaining the original shape either during unloading (superelastic or pseudo-elastic (PE) effect) or through a thermal cycle (shape-memory effect (SME)) [1,2]. Since such effects are in general not present in standard alloys, SMAs are often used in innovative applications. For example, nowadays pseudo-elastic Nitinol is a common and well-known engineering material in the medical industry [3,4].

The origin of SMA features is a reversible thermo-elastic martensitic phase transformation between a high symmetry, austenitic phase and a low symmetry, martensitic phase. Austenite is a solid phase, usually characterized by a body-centered cubic crystallographic structure, which transforms into martensite by means of a lattice shearing mechanism. When the transformation is driven by a temperature decrease, martensite variants compensate each other, resulting in no macroscopic deformation. However, when the transformation is driven by the application of a load, specific martensite variants, favorable to the applied stress, are preferentially formed, exhibiting a macroscopic shape change in the direction of the applied stress. Upon unloading or heating, this shape change disappears through the reversible conversion of the martensite variants into the parent phase [1,5].

For a stress-free SMA material, four characteristic temperatures can be identified, defined as the starting and finishing temperatures during forward transformation (austenite to martensite), M_s and M_f, and as the starting and finishing temperatures during reverse transformation, A_s and A_f. Accordingly, in a stress-free condition, at a temperature above A_f, only the austenitic phase is stable, while at a temperature below M_f, only the martensitic phase is stable. As a consequence, applying a stress at a temperature above A_f, SMAs exhibit a pseudo-elastic behavior with a full recovery of inelastic strain upon unloading, while at a temperature below M_s, the material presents the shape-memory effect with permanent inelastic strains upon unloading which may be recovered by heating.

In most applications, SMAs experience a general thermo-mechanical loading conditions more complicated than uniaxial or

* Corresponding author. Tel.: +98 21 6616 5511; fax: +98 21 6600 0021.
E-mail address: arghavani@mech.sharif.ir (J. Arghavani).
[1] Currently visiting Ph.D. student, Dipartimento di Meccanica Strutturale, Università degli Studi di Pavia, Italy.

0168-874X/$ - see front matter © 2010 Elsevier B.V. All rights reserved.
doi:10.1016/j.finel.2010.09.001

multiaxial proportional loadings, typically undergoing very large rotations and moderate strains (i.e., in the range of 10% for polycrystals [1]). For example, with reference to biomedical applications, stent structures are usually designed to significantly reduce their diameter during the insertion into a catheter; thereby, large rotations combined with moderate strains occur and the use of a finite deformation scheme is preferred.

The majority of the currently available 3D macroscopic constitutive models for SMAs has been developed in the small deformation regime (see, e.g., [6–16] among others). Finite deformation SMA constitutive models proposed in the literature have been mainly developed by extending small strain models. The approach in most cases is based on the multiplicative decomposition of the deformation gradient into an elastic and an inelastic or transformation part [17–25], though there are some models which have utilized an additive decomposition of the strain rate tensor into an elastic and an inelastic part [26].

In the present work we focus on a finite-strain extension of the small-strain constitutive model initially proposed by Souza et al. [8] and extensively studied in Refs. [27–29]. We first develop a finite-strain constitutive model containing an asymmetric tensor, also observed in the constitutive equations of [20–24]. To this end, we propose an improved alternative constitutive model which is expressed in terms of symmetric tensors only. We then implement the proposed model in a user-defined subroutine (UMAT) in the nonlinear finite element software ABAQUS/Standard and compare the solution CPU times for different boundary value problems. The results show the increased computational efficiency (in terms of solution CPU time), when the proposed alternative symmetric form is used. This is mostly due to the simplification in computing fourth-order tensors appearing when a tensorial equation is linearized.

The structure of the paper is as follows. In Section 2, based on a multiplicative decomposition of the deformation gradient into elastic and transformation parts, we present the time-continuous finite-strain constitutive model. In Section 3, we propose an alternative constitutive equation which includes only symmetric tensors. In Section 4, based on an exponential mapping, the time-discrete form and the solution algorithm are discussed. In Section 5, implementing the proposed integration algorithm within the commercial nonlinear finite element software ABAQUS/Standard, we simulate different boundary value problems. We finally draw conclusions in Section 6.

2. A 3D finite-strain SMA constitutive model: time-continuous frame

We use a multiplicative decomposition of the deformation gradient and present a thermodynamically consistent finite strain constitutive model as done by Reese and Christ [20,21], Evangelista et al. [22] and, more recently, by Arghavani et al. [23,24]. The finite-strain constitutive model takes its origin from the small-strain constitutive model proposed by Souza et al. [8] and improved and discussed by Auricchio and Petrini [27–29].

2.1. Constitutive model development

Considering a deformable body, we denote with $\boldsymbol{F}$ the deformation gradient and with J its determinant, supposed to be positive. The tensor $\boldsymbol{F}$ can be uniquely decomposed as

$$\boldsymbol{F}=\boldsymbol{R}\boldsymbol{U}=\boldsymbol{V}\boldsymbol{R} \tag{1}$$

where $\boldsymbol{U}$ and $\boldsymbol{V}$ are the right and left stretch tensors, respectively, both positive definite and symmetric, while $\boldsymbol{R}$ is a proper orthogonal rotation tensor. The right and left Cauchy–Green deformation tensors are then, respectively, defined as

$$\boldsymbol{C}=\boldsymbol{F}^T\boldsymbol{F},\quad \boldsymbol{b}=\boldsymbol{F}\boldsymbol{F}^T \tag{2}$$

and the Green–Lagrange strain tensor, $\boldsymbol{E}$, reads as

$$\boldsymbol{E}=\frac{\boldsymbol{C}-\boldsymbol{1}}{2} \tag{3}$$

where $\boldsymbol{1}$ is the second-order identity tensor. Moreover, the velocity gradient tensor $\boldsymbol{l}$ is given as

$$\boldsymbol{l}=\dot{\boldsymbol{F}}\boldsymbol{F}^{-1} \tag{4}$$

The symmetric and anti-symmetric parts of $\boldsymbol{l}$ supply the strain rate tensor $\boldsymbol{d}$ and the vorticity tensor $\boldsymbol{w}$, i.e.,

$$\boldsymbol{d}=\tfrac{1}{2}(\boldsymbol{l}+\boldsymbol{l}^T),\quad \boldsymbol{w}=\tfrac{1}{2}(\boldsymbol{l}-\boldsymbol{l}^T) \tag{5}$$

Taking the time derivative of Eq. (3) and using (4) and (5), it can be shown that

$$\dot{\boldsymbol{E}}=\boldsymbol{F}^T\boldsymbol{d}\boldsymbol{F} \tag{6}$$

Following a well-established approach adopted in plasticity [30,31] and already used for SMAs [17–24], we assume a local multiplicative decomposition of the deformation gradient into an elastic part $\boldsymbol{F}^e$, defined with respect to an intermediate configuration, and a transformation one $\boldsymbol{F}^t$, defined with respect to the reference configuration. Accordingly,

$$\boldsymbol{F}=\boldsymbol{F}^e\boldsymbol{F}^t \tag{7}$$

Since experimental evidences indicate that the transformation flow is nearly isochoric, we impose $\det(\boldsymbol{F}^t)=1$, which after taking the time derivative results in

$$\mathrm{tr}(\boldsymbol{d}^t)=0 \tag{8}$$

We define $\boldsymbol{C}^e=\boldsymbol{F}^{e^T}\boldsymbol{F}^e$ and $\boldsymbol{C}^t=\boldsymbol{F}^{t^T}\boldsymbol{F}^t$ as the elastic and the transformation right Cauchy–Green deformation tensors, respectively, and using definitions (2) and (7), we obtain

$$\boldsymbol{C}^e=\boldsymbol{F}^{t^{-T}}\boldsymbol{C}\boldsymbol{F}^{t^{-1}} \tag{9}$$

To satisfy the principle of material objectivity, the Helmholtz free energy has to depend on $\boldsymbol{F}^e$ only through the elastic right Cauchy–Green deformation tensor; it is moreover assumed to be a function of the transformation right Cauchy–Green deformation tensor and of the temperature, T, in the following form [22–24]

$$\Psi=\Psi(\boldsymbol{C}^e,\boldsymbol{C}^t,T)=\psi^e(\boldsymbol{C}^e)+\psi^t(\boldsymbol{E}^t,T) \tag{10}$$

where $\psi^e(\boldsymbol{C}^e)$ is a hyperelastic strain energy function and $\boldsymbol{E}^t=(\boldsymbol{C}^t-\boldsymbol{1})/2$ is the transformation strain. We remark that in proposing decomposition (10), we have assumed the same material behavior for the austenite and martensite phases. In addition, we assume $\psi^e(\boldsymbol{C}^e)$ to be an isotropic function of $\boldsymbol{C}^e$; it can be therefore expressed as

$$\psi^e(\boldsymbol{C}^e)=\psi^e(I_{\boldsymbol{C}^e},II_{\boldsymbol{C}^e},III_{\boldsymbol{C}^e}) \tag{11}$$

where $I_{\boldsymbol{C}^e},II_{\boldsymbol{C}^e},III_{\boldsymbol{C}^e}$ are the invariants of $\boldsymbol{C}^e$. We also define ψ^t in the following form [8,22,27–29]

$$\psi^t(\boldsymbol{E}^t,T)=\tau_M(T)\|\boldsymbol{E}^t\|+\tfrac{1}{2}h\|\boldsymbol{E}^t\|^2+\mathcal{I}_{\varepsilon_L}(\|\boldsymbol{E}^t\|) \tag{12}$$

where $\tau_M(T)=\beta\langle T-T_0\rangle$ and β, T_0 and h are material parameters; the MacCauley brackets calculate the positive part of the argument, i.e., $\langle x\rangle=(x+|x|)/2$, and the norm operator is defined as $\|\boldsymbol{A}\|=\sqrt{\boldsymbol{A}:\boldsymbol{A}^T}$, with $\boldsymbol{A}:\boldsymbol{B}=A_{ij}B_{ij}$.

Moreover, in Eq. (12) we also use the indicator function $\mathcal{I}_{\varepsilon_L}$ defined as

$$\mathcal{I}_{\varepsilon_L}(\|\boldsymbol{E}^t\|)=\begin{cases}0 & \text{if } \|\boldsymbol{E}^t\|\le\varepsilon_L\\ +\infty & \text{otherwise}\end{cases} \tag{13}$$

to satisfy the constraint on the transformation strain norm (i.e., $\|\boldsymbol{E}^t\| \le \varepsilon_L$). The material parameter ε_L is the maximum transformation strain norm in a uniaxial test.

Taking the time derivative of Eq. (9) and using (4), the material time derivative of the elastic right Cauchy–Green deformation tensor is obtained as

$$\dot{\boldsymbol{C}}^e = -\boldsymbol{l}^{t^T}\boldsymbol{C}^e + \boldsymbol{F}^{t^{-T}}\dot{\boldsymbol{C}}\boldsymbol{F}^{t^{-1}} - \boldsymbol{C}^e\boldsymbol{l}^t \tag{14}$$

We now use the Clausius–Duhem inequality form of the second law of thermodynamics

$$\boldsymbol{S} : \tfrac{1}{2}\dot{\boldsymbol{C}} - (\dot{\Psi} + \eta\dot{T}) \ge 0 \tag{15}$$

where $\boldsymbol{S}$ is the second Piola–Kirchhoff stress tensor related to the Cauchy stress $\boldsymbol{\sigma}$ through

$$\boldsymbol{S} = J\boldsymbol{F}^{-1}\boldsymbol{\sigma}\boldsymbol{F}^{-T} \tag{16}$$

and η is the entropy. Substituting (10) into (15), we obtain

$$\boldsymbol{S} : \frac{1}{2}\dot{\boldsymbol{C}} - \left(\frac{\partial\psi^e}{\partial\boldsymbol{C}^e} : \dot{\boldsymbol{C}}^e + \frac{\partial\psi^t}{\partial\boldsymbol{E}^t} : \dot{\boldsymbol{E}}^t + \frac{\partial\psi^t}{\partial T}\dot{T}\right) - \eta\dot{T} \ge 0 \tag{17}$$

Now, substituting (14) into (17), after some mathematical manipulations, we obtain

$$\left(\boldsymbol{S} - 2\boldsymbol{F}^{t^{-1}}\frac{\partial\psi^e}{\partial\boldsymbol{C}^e}\boldsymbol{F}^{t^{-T}}\right) : \frac{1}{2}\dot{\boldsymbol{C}} + 2\boldsymbol{C}^e\frac{\partial\psi^e}{\partial\boldsymbol{C}^e} : \boldsymbol{l}^t - \boldsymbol{X} : \dot{\boldsymbol{E}}^t - \left(\eta + \frac{\partial\psi^t}{\partial T}\right)\dot{T} \ge 0 \tag{18}$$

where

$$\boldsymbol{X} = h\boldsymbol{E}^t + (\tau_M(T) + \gamma)\boldsymbol{N} \tag{19}$$

and

$$\boldsymbol{N} = \frac{\boldsymbol{E}^t}{\|\boldsymbol{E}^t\|} \tag{20}$$

The positive variable γ results from the indicator function subdifferential $\partial\mathcal{I}_{\varepsilon_L}(\|\boldsymbol{E}^t\|)$ and it is such that

$$\begin{cases} \gamma \ge 0 & \text{if } \|\boldsymbol{E}^t\| = \varepsilon_L \\ \gamma = 0 & \text{otherwise} \end{cases} \tag{21}$$

In deriving (18) we have used the isotropic property of $\psi^e(\boldsymbol{C}^e)$, implying that $\boldsymbol{C}^e$ and $\partial\psi^e/\partial\boldsymbol{C}^e$ are coaxial. Following standard arguments, we finally conclude that

$$\begin{cases} \boldsymbol{S} = 2\boldsymbol{F}^{t^{-1}}\dfrac{\partial\psi^e}{\partial\boldsymbol{C}^e}\boldsymbol{F}^{t^{-T}} \\ \eta = -\dfrac{\partial\psi^t}{\partial T} \end{cases} \tag{22}$$

Using a property of second-order tensor double contraction, i.e., $\boldsymbol{A} : (\boldsymbol{B}\boldsymbol{C}) = \boldsymbol{B} : (\boldsymbol{A}\boldsymbol{C}^T) = \boldsymbol{C} : (\boldsymbol{B}^T\boldsymbol{A})$, we obtain

$$\boldsymbol{X} : \dot{\boldsymbol{E}}^t = (\boldsymbol{F}^t\boldsymbol{X}\boldsymbol{F}^{t^T}) : \boldsymbol{d}^t \tag{23}$$

In deriving (23) we have used the following relation:

$$\dot{\boldsymbol{E}}^t = \boldsymbol{F}^{t^T}\boldsymbol{d}^t\boldsymbol{F}^t \tag{24}$$

Substituting (22) and (23) into (18) and taking advantage of the symmetry of $\boldsymbol{C}^e(\partial\psi^e/\partial\boldsymbol{C}^e)$, the dissipation inequality can be written as

$$(\boldsymbol{P} - \boldsymbol{K}) : \boldsymbol{d}^t \ge 0 \tag{25}$$

where

$$\begin{cases} \boldsymbol{P} = 2\boldsymbol{C}^e\dfrac{\partial\psi^e}{\partial\boldsymbol{C}^e} \\ \boldsymbol{K} = \boldsymbol{F}^t\boldsymbol{X}\boldsymbol{F}^{t^T} \end{cases} \tag{26}$$

To satisfy the second law of thermodynamics, (25), we define the following evolution equation:

$$\boldsymbol{d}^t = \dot{\zeta}\frac{(\boldsymbol{P} - \boldsymbol{K})^D}{\|(\boldsymbol{P} - \boldsymbol{K})^D\|} \tag{27}$$

where we denote with a superscript D the deviatoric part of a tensor. Moreover, we highlight that (27) satisfies the inelastic deformation incompressibility condition (8).

To describe phase transformation, we choose the following limit function:

$$f = \|(\boldsymbol{P} - \boldsymbol{K})^D\| - R \tag{28}$$

where the material parameter R is the elastic region radius. Similarly to plasticity, we also introduce the consistency parameter and the limit function satisfying the Kuhn–Tucker conditions

$$f \le 0, \quad \dot{\zeta} \ge 0, \quad \dot{\zeta}f = 0 \tag{29}$$

2.2. Representation with respect to the reference configuration

In the previous section, using a multiplicative decomposition of the deformation gradient into elastic and transformation parts, we derived a finite-strain constitutive model. However, while $\boldsymbol{F}$ and $\boldsymbol{F}^t$ are defined with respect to the reference configuration, $\boldsymbol{F}^e$ is defined with respect to an intermediate configuration. It is then necessary to recast all equations in terms of $\boldsymbol{C}$ (control variable) and $\boldsymbol{C}^t$ (internal variable) which are described with respect to the reference configuration, allowing to express all equations in a Lagrangian form.

Since a hyperelastic strain energy function ψ^e has been introduced in terms of $\boldsymbol{C}^e$ (i.e., with respect to the intermediate configuration), we first investigate it.

As introduced in (11), ψ^e depends on $\boldsymbol{C}^e$ only through its invariants, which are equal to those of $\boldsymbol{C}\boldsymbol{C}^{t^{-1}}$. In fact, for the first invariant the following identity holds

$$\begin{aligned} I_{\boldsymbol{C}^e} &= \mathrm{tr}(\boldsymbol{C}^e) = \mathrm{tr}(\boldsymbol{F}^{t^{-T}}\boldsymbol{C}\boldsymbol{F}^{t^{-1}}) = \mathrm{tr}\,(\boldsymbol{C}\boldsymbol{F}^{t^{-1}}\boldsymbol{F}^{t^{-T}}) \\ &= \mathrm{tr}(\boldsymbol{C}\boldsymbol{C}^{t^{-1}}) = I_{\boldsymbol{C}\boldsymbol{C}^{t^{-1}}} \end{aligned} \tag{30}$$

and similar relations hold for the second and the third invariants.

Accordingly, we may write

$$\frac{\partial\psi^e}{\partial\boldsymbol{C}^e} = \alpha_1\boldsymbol{1} + \alpha_2\boldsymbol{C}^e + \alpha_3\boldsymbol{C}^{e^2} \tag{31}$$

where $\alpha_i = \alpha_i(I_{\boldsymbol{C}\boldsymbol{C}^{t^{-1}}}, II_{\boldsymbol{C}\boldsymbol{C}^{t^{-1}}}, III_{\boldsymbol{C}\boldsymbol{C}^{t^{-1}}})$. Substituting (31) into $(22)_1$ and using (9), we conclude that

$$\boldsymbol{S} = 2(\alpha_1\boldsymbol{C}^{t^{-1}} + \alpha_2\boldsymbol{C}^{t^{-1}}\boldsymbol{C}\boldsymbol{C}^{t^{-1}} + \alpha_3\boldsymbol{C}^{t^{-1}}(\boldsymbol{C}\boldsymbol{C}^{t^{-1}})^2) \tag{32}$$

which expresses the second Piola–Kirchhoff stress tensor in terms of quantities computed with respect to the reference configuration.

In order to find the Lagrangian form of the evolution equation, we substitute (27) into (24) and obtain

$$\dot{\boldsymbol{E}}^t = \dot{\zeta}\boldsymbol{F}^{t^T}\frac{(\boldsymbol{P} - \boldsymbol{K})^D}{\|(\boldsymbol{P} - \boldsymbol{K})^D\|}\boldsymbol{F}^t \tag{33}$$

or equivalently,

$$\dot{\boldsymbol{C}}^t = 2\dot{\zeta}\boldsymbol{F}^{t^T}\frac{(\boldsymbol{P} - \boldsymbol{K})^D}{\|(\boldsymbol{P} - \boldsymbol{K})^D\|}\boldsymbol{F}^t \tag{34}$$

Focusing on the first term of the right hand side of Eq. (34), we may observe that

$$\boldsymbol{F}^{t^T}\boldsymbol{P}\boldsymbol{F}^t = (\boldsymbol{F}^t\boldsymbol{C}^e\boldsymbol{F}^t)\left(2\boldsymbol{F}^{t^{-1}}\frac{\partial\psi^e}{\partial\boldsymbol{C}^e}\boldsymbol{F}^{t^{-T}}\right)\boldsymbol{C}^t = \boldsymbol{C}\boldsymbol{S}\boldsymbol{C}^t \tag{35}$$

while, focusing on the second term of the right hand side of Eq. (34), we may observe that

$$\boldsymbol{F}^{t^T}\boldsymbol{K}\boldsymbol{F}^t = \boldsymbol{F}^{t^T}\boldsymbol{F}^t\boldsymbol{X}\boldsymbol{F}^{t^T}\boldsymbol{F}^t = \boldsymbol{C}^t\boldsymbol{X}\boldsymbol{C}^t \tag{36}$$

We may then conclude that

$$\boldsymbol{F}^{t^T}(\boldsymbol{P}-\boldsymbol{K})\boldsymbol{F}^t = \boldsymbol{Y}\boldsymbol{C}^t \tag{37}$$

and obtain from (35)–(37)

$$\boldsymbol{Y} = \boldsymbol{C}\boldsymbol{S}-\boldsymbol{C}^t\boldsymbol{X} \tag{38}$$

Moreover, we have

$$\begin{aligned}\boldsymbol{F}^{t^T}(\boldsymbol{P}-\boldsymbol{K})^D\boldsymbol{F}^t &= \boldsymbol{F}^{t^T}(\boldsymbol{P}-\boldsymbol{K}-\tfrac{1}{3}\mathrm{tr}(\boldsymbol{P}-\boldsymbol{K})\boldsymbol{1})\boldsymbol{F}^t \\ &= (\boldsymbol{C}\boldsymbol{S}\boldsymbol{C}^t-\boldsymbol{C}^t\boldsymbol{X}\boldsymbol{C}^t-\tfrac{1}{3}\mathrm{tr}(\boldsymbol{C}\boldsymbol{S})\boldsymbol{C}^t+\tfrac{1}{3}\mathrm{tr}(\boldsymbol{C}^t\boldsymbol{X})\boldsymbol{C}^t) = \boldsymbol{Y}^D\boldsymbol{C}^t\end{aligned} \tag{39}$$

yielding

$$(\boldsymbol{P}-\boldsymbol{K})^D = \boldsymbol{F}^{t^{-T}}\boldsymbol{Y}^D\boldsymbol{F}^{t^T} \tag{40}$$

and

$$\|(\boldsymbol{P}-\boldsymbol{K})^D\| = \|\boldsymbol{Y}^D\| \tag{41}$$

Now, we substitute (40) and (41) into (28) and (33) to obtain

$$f = \|\boldsymbol{Y}^D\|-R \tag{42}$$

and

$$\dot{\boldsymbol{C}}^t = 2\dot{\zeta}\frac{\boldsymbol{Y}^D}{\|\boldsymbol{Y}^D\|}\boldsymbol{C}^t \tag{43}$$

Table 1 presents the time-continuous finite-strain constitutive model expressed only in terms of Lagrangian quantities, which has already been presented in [22,24].

3. An alternative form of the constitutive model in terms of symmetric quantities

We observe that due to the asymmetry of $\boldsymbol{CS}$, the quantity $\boldsymbol{Y}$ is not symmetric. The asymmetric tensor $\boldsymbol{Y}$ also appears in the constitutive equations proposed in [20–24]. To this end, we present an alternative formulation which is in terms of symmetric tensors only. According to (32), we may write

$$\boldsymbol{C}\boldsymbol{S} = 2(\alpha_1\boldsymbol{C}\boldsymbol{C}^{t^{-1}}+\alpha_2(\boldsymbol{C}\boldsymbol{C}^{t^{-1}})^2+\alpha_3(\boldsymbol{C}\boldsymbol{C}^{t^{-1}})^3) \tag{44}$$

Eq. (44) shows that the asymmetry in $\boldsymbol{CS}$ is due to the asymmetric term $\boldsymbol{C}\boldsymbol{C}^{t^{-1}}$. We now present the following identity:

$$\boldsymbol{C}\boldsymbol{C}^{t^{-1}} = \boldsymbol{U}^t(\boldsymbol{U}^{t^{-1}}\boldsymbol{C}\boldsymbol{U}^{t^{-1}})\boldsymbol{U}^{t^{-1}} = \boldsymbol{U}^t\overline{\boldsymbol{C}}\boldsymbol{U}^{t^{-1}} \tag{45}$$

where

$$\overline{\boldsymbol{C}} = \boldsymbol{U}^{t^{-1}}\boldsymbol{C}\boldsymbol{U}^{t^{-1}} \tag{46}$$

Substituting (45) into (44), we obtain

$$\boldsymbol{C}\boldsymbol{S} = \boldsymbol{U}^t\overline{\boldsymbol{C}}\,\overline{\boldsymbol{S}}\boldsymbol{U}^{t^{-1}} \tag{47}$$

where

$$\overline{\boldsymbol{S}} = 2(\alpha_1\boldsymbol{1}+\alpha_2\overline{\boldsymbol{C}}+\alpha_3\overline{\boldsymbol{C}}^2) \tag{48}$$

Moreover, due to the coaxiality of $\boldsymbol{C}^t$ and $\boldsymbol{X}$, we may write

$$\boldsymbol{C}^t\boldsymbol{X} = \boldsymbol{U}^t\boldsymbol{C}^t\boldsymbol{X}\boldsymbol{U}^{t^{-1}} \tag{49}$$

Substituting (47) and (49) into (38), we obtain

$$\boldsymbol{Y} = \boldsymbol{U}^t\boldsymbol{Q}\boldsymbol{U}^{t^{-1}} \tag{50}$$

where $\boldsymbol{Q}$ is defined as

$$\boldsymbol{Q} = \overline{\boldsymbol{C}}\,\overline{\boldsymbol{S}}-\boldsymbol{C}^t\boldsymbol{X} \tag{51}$$

Using the property $\mathrm{tr}(\boldsymbol{U}^t\boldsymbol{Q}\boldsymbol{U}^{t^{-1}}) = \mathrm{tr}(\boldsymbol{Q})$, we also obtain

$$\boldsymbol{Y}^D = \boldsymbol{U}^t\boldsymbol{Q}^D\boldsymbol{U}^{t^{-1}} \tag{52}$$

We now substitute (52) into (42) and (43) and obtain (53) and (54), respectively, as follows:

$$\boldsymbol{Y}^D:\boldsymbol{Y}^{D^T} = \boldsymbol{Q}^D:\boldsymbol{Q}^D \quad \text{or} \quad f = \|\boldsymbol{Y}^D\|-R = \|\boldsymbol{Q}^D\|-R \tag{53}$$

and

$$\dot{\boldsymbol{C}}^t = 2\dot{\zeta}\boldsymbol{U}^t\frac{\boldsymbol{Q}^D}{\|\boldsymbol{Q}^D\|}\boldsymbol{U}^t \tag{54}$$

We remark that in the proposed formulation we can express $\boldsymbol{S}$ as

$$\boldsymbol{S} = \boldsymbol{U}^{t^{-1}}\overline{\boldsymbol{S}}\boldsymbol{U}^{t^{-1}} \tag{55}$$

Finally, we summarize the proposed improved time-continuous finite-strain constitutive models in Table 2.

We may compare the original and the proposed alternative time-continuous forms summarized in Tables 1 and 2, respectively. It is clearly observed that in the proposed alternative constitutive model, all quantities are symmetric and the norm operator argument is also a symmetric tensor.

Remark 1. We note that according to (20), the variable $\boldsymbol{N}$ is not defined for the case of vanishing transformation strain. To this end, we use a regularization scheme proposed by Helm and Haupt [9] and also used in [7,20,21] to overcome this problem:

$$\overline{\|\boldsymbol{E}^t\|} = \sqrt{\|\boldsymbol{E}^t\|^2+\delta} \tag{56}$$

where δ is a user-defined parameter (typical value: 10^{-7}).

4. A 3D finite-strain SMA constitutive model: time-discrete frame

In this section we investigate the numerical solution of the constitutive model derived in Section 3 and summarized in Table 2, with the final goal of using it within a finite element program. The main task is to apply an appropriate numerical time-integration scheme to the evolution equation of the internal variable, considering that, in general, implicit schemes are

Table 1
Finite-strain constitutive model in the time-continuous frame: original form [22,24].

External variables: $\boldsymbol{C}, T$
Internal variable: $\boldsymbol{C}^t$
Stress quantities:
$\boldsymbol{S} = 2\alpha_1\boldsymbol{C}^{t^{-1}}+2\alpha_2\boldsymbol{C}^{t^{-1}}\boldsymbol{C}\boldsymbol{C}^{t^{-1}}$
$\quad+2\alpha_3\boldsymbol{C}^{t^{-1}}(\boldsymbol{C}\boldsymbol{C}^{t^{-1}})^2$
$\boldsymbol{Y} = \boldsymbol{C}\boldsymbol{S}-\boldsymbol{C}^t\boldsymbol{X}$
$\boldsymbol{X} = h\boldsymbol{E}^t+(\tau_M+\gamma)\boldsymbol{N}$
with
$\begin{cases}\gamma\geq 0 & \text{if}\|\boldsymbol{E}^t\| = \varepsilon_L \\ \gamma = 0 & \text{otherwise}\end{cases}$
and
$\boldsymbol{N} = \frac{\boldsymbol{E}^t}{\|\boldsymbol{E}^t\|}$
where $\boldsymbol{E}^t = (\boldsymbol{C}^t-\boldsymbol{1})/2$
Evolution equation:
$\dot{\boldsymbol{C}}^t = 2\dot{\zeta}\frac{\boldsymbol{Y}^D}{\|\boldsymbol{Y}^D\|}\boldsymbol{C}^t$
Limit function:
$f = \|\boldsymbol{Y}^D\|-R$
Kuhn–Tucker conditions:
$f\leq 0, \dot{\zeta}\geq 0, \dot{\zeta}f = 0$
Norm operator:
$\|\boldsymbol{Y}^D\| = \sqrt{\boldsymbol{Y}^D:\boldsymbol{Y}^{D^T}}$

Table 2
Finite-strain constitutive model in the time-continuous frame: proposed alternative form.

External variables: $\boldsymbol{C}, T$
Internal variable: $\boldsymbol{C}^t$
Stress quantities:
$\boldsymbol{S}=\boldsymbol{U}^{t^{-1}}\overline{\boldsymbol{S}}\boldsymbol{U}^{t^{-1}}$
$\overline{\boldsymbol{S}}=2(\alpha_1\boldsymbol{1}+\alpha_2\overline{\boldsymbol{C}}+\alpha_3\overline{\boldsymbol{C}}^2)$
$\boldsymbol{Q}=\overline{\boldsymbol{C}}\,\overline{\boldsymbol{S}}-\boldsymbol{C}^t\boldsymbol{X}$
$\boldsymbol{X}=h\boldsymbol{E}^t+(\tau_M+\gamma)\boldsymbol{N}$
with
$\begin{cases}\gamma\geq 0 & \text{if } \|\boldsymbol{E}^t\|=\varepsilon_L\\ \gamma=0 & \text{otherwise}\end{cases}$
and
$\boldsymbol{N}=\frac{\boldsymbol{E}^t}{\|\boldsymbol{E}^t\|}, \overline{\boldsymbol{C}}=\boldsymbol{U}^{t^{-1}}\boldsymbol{C}\boldsymbol{U}^{t^{-1}}$
where $\boldsymbol{E}^t=(\boldsymbol{C}^t-\boldsymbol{1})/2$
Evolution equation:
$\dot{\boldsymbol{C}}^t=2\dot{\zeta}\boldsymbol{U}^t\frac{\boldsymbol{Q}^D}{\|\boldsymbol{Q}^D\|}\boldsymbol{U}^t$
Limit function:
$f=\|\boldsymbol{Q}^D\|-R$
Kuhn–Tucker conditions:
$f\leq 0, \dot{\zeta}\geq 0, \dot{\zeta}f=0$
Norm operator:
$\|\boldsymbol{Q}^D\|=\sqrt{\boldsymbol{Q}^D:\boldsymbol{Q}^D}$

preferred because of their stability at larger time step sizes. Moreover, the present section provides some details about the stress update and the computation of the consistent tangent matrix, which are the two points where the material model is directly connected to the finite element solution procedure.

We treat the nonlinear problem described in Section 3 as an implicit time-discrete deformation-driven problem. Accordingly, we subdivide the time interval of interest $[0, t]$ in sub-increments and we solve the evolution problem over the generic interval $[t_n,t_{n+1}]$ with $t_{n+1}>t_n$. To simplify the notation, we indicate with the subscript n a quantity evaluated at time t_n, and with no subscript a quantity evaluated at time t_{n+1}.Assuming to know the solution and the deformation gradient $\boldsymbol{F}_n$ at time t_n as well as the deformation gradient $\boldsymbol{F}$ at time t_{n+1}, the stress and the internal variable have to be updated from the deformation history.

4.1. Time integration

Exponential-based integration schemes are frequently applied to problems in plasticity and isotropic inelasticity [32,33], since the use of the exponential mapping allows to exactly conserve the volume during an inelastic deformation. Thus, larger time step sizes than any other first-order accurate integration scheme may be used.

We now consider an evolution equation in the following form:

$$\dot{\boldsymbol{C}}^t=\dot{\zeta}\boldsymbol{A}=\dot{\zeta}\boldsymbol{A}_1\boldsymbol{C}^t \tag{57}$$

where $\boldsymbol{A}_1=\boldsymbol{A}\boldsymbol{C}^{t^{-1}}$ with $\boldsymbol{A}$ being a symmetric tensor, while $\boldsymbol{A}_1$ is not symmetric in general.

Applying the exponential mapping scheme to the evolution equation (57), we obtain

$$\boldsymbol{C}^t=\exp(\Delta\zeta\boldsymbol{A}_1)\boldsymbol{C}_n^t \tag{58}$$

In the equation above, we need to compute the exponential of an asymmetric tensor, which is a problematic computation due to the impossibility of using a spectral decomposition method.[2]

[2] The exponent of an asymmetric tensor is computed with a series expansion. However, the exponent of a symmetric tensor can also be computed in closed form by means of a spectral decomposition.

Accordingly, using the strategy initially proposed in [20–22,34] and also exploited in [35,24], we can find an alternative expression where the argument of the exponential operator is a symmetric tensor which can be computed through spectral decomposition. Following [20], we can write

$$\begin{aligned}\exp(\Delta\zeta\boldsymbol{A}_1)&=\boldsymbol{1}+\Delta\zeta\boldsymbol{A}_1+\frac{\Delta\zeta^2}{2!}\boldsymbol{A}_1^2+\cdots\\&=\boldsymbol{1}+\Delta\zeta\boldsymbol{A}\boldsymbol{C}^{t^{-1}}+\frac{\Delta\zeta^2}{2!}(\boldsymbol{A}\boldsymbol{C}^{t^{-1}})^2+\cdots\\&=\boldsymbol{U}^t\left(\boldsymbol{1}+\Delta\zeta\boldsymbol{U}^{t^{-1}}\boldsymbol{A}\boldsymbol{U}^{t^{-1}}+\frac{\Delta\zeta^2}{2!}(\boldsymbol{U}^{t^{-1}}\boldsymbol{A}\boldsymbol{U}^{t^{-1}})^2+\cdots\right)\boldsymbol{U}^{t^{-1}}\\&=\boldsymbol{U}^t\exp(\Delta\zeta\boldsymbol{U}^{t^{-1}}\boldsymbol{A}\boldsymbol{U}^{t^{-1}})\boldsymbol{U}^{t^{-1}}\end{aligned} \tag{59}$$

We now right- and left-multiply (58) by $\boldsymbol{C}_n^{t^{-1}}$ and $\boldsymbol{C}^{t^{-1}}$, respectively, to obtain

$$\boldsymbol{C}_n^{t^{-1}}=\boldsymbol{C}^{t^{-1}}\exp(\Delta\zeta\boldsymbol{A}_1) \tag{60}$$

Then, substituting (59) into (60), we can write the integration formula as

$$-\boldsymbol{C}_n^{t^{-1}}+\boldsymbol{U}^{t^{-1}}\exp(\Delta\zeta\boldsymbol{U}^{t^{-1}}\boldsymbol{A}\boldsymbol{U}^{t^{-1}})\boldsymbol{U}^{t^{-1}}=\boldsymbol{0} \tag{61}$$

which is the time-discrete form associated to (57) presented so far in the literature [20–22,34,35,24].

Comparing (54) and (57), we conclude that

$$\boldsymbol{A}=2\boldsymbol{U}^t\frac{\boldsymbol{Q}^D}{\|\boldsymbol{Q}^D\|}\boldsymbol{U}^t \tag{62}$$

We now substitute (62) into (61) and after right- and left-multiplying by $\boldsymbol{U}^t$, we obtain the time-discrete form of the proposed evolution Eq. (54) as

$$-\boldsymbol{U}^t\boldsymbol{C}_n^{t^{-1}}\boldsymbol{U}^t+\exp(2\Delta\zeta\boldsymbol{W})=\boldsymbol{0} \tag{63}$$

where

$$\boldsymbol{W}=\frac{\boldsymbol{Q}^D}{\|\boldsymbol{Q}^D\|} \tag{64}$$

4.2. Solution algorithm

As usual in computational inelasticity problems, to solve the time-discrete constitutive model we use an elastic predictor-inelastic corrector procedure. The algorithm consists of evaluating an elastic trial state, in which the internal variable remains constant, and of verifying the admissibility of the trial function. If the trial state is admissible, the step is elastic; otherwise, the step is inelastic and the transformation internal variable has to be updated through integration of the evolution equation.

In order to solve the inelastic step, we use another predictor-corrector scheme, that is, we assume $\gamma=0$ (i.e., we predict an unsaturated transformation strain case with $\|\boldsymbol{E}^t\|\leq\varepsilon_L$) and we solve the following system of nonlinear equations (we refer to this system as *PT* 1 system):

$$\begin{cases}\boldsymbol{R}^t=-\boldsymbol{U}^t\boldsymbol{C}_n^{t^{-1}}\boldsymbol{U}^t+\exp(2\Delta\zeta\boldsymbol{W})=\boldsymbol{0}\\ R^\zeta=\|\boldsymbol{Q}^D\|-R=0\end{cases} \tag{65}$$

If the solution is not admissible (i.e., $\|\boldsymbol{E}^t\|_{PT1}>\varepsilon_L$), we assume $\gamma\geq 0$ (i.e., we consider a saturated transformation case with $\|\boldsymbol{E}^t\|=\varepsilon_L$) and we solve the following system of nonlinear equations (we refer to this system as *PT2* system):

$$\begin{cases}\boldsymbol{R}^t=-\boldsymbol{U}^t\boldsymbol{C}_n^{t^{-1}}\boldsymbol{U}^t+\exp(2\Delta\zeta\boldsymbol{W})=\boldsymbol{0}\\ R^\zeta=\|\boldsymbol{Q}^D\|-R=0\\ R^\gamma=\|\boldsymbol{E}^t\|-\varepsilon_L=0\end{cases} \tag{66}$$

The solution of Eqs. (65) and (66) is, in general, approached through a straightforward Newton-Raphson method.

Remark 2. The corresponding *PT* 1 and *PT* 2 systems for the original form of the constitutive model are, respectively, as follows [22,24]:

$$\begin{cases} \boldsymbol{R}^t = -\boldsymbol{C}_n^{t^{-1}} + \boldsymbol{U}^{t^{-1}} \exp(\Delta\zeta \boldsymbol{U}^{t^{-1}} \boldsymbol{A} \boldsymbol{U}^{t^{-1}}) \boldsymbol{U}^{t^{-1}} = \boldsymbol{0} \\ R^\zeta = \|\boldsymbol{Y}^D\| - R = 0 \end{cases} \tag{67}$$

$$\begin{cases} \boldsymbol{R}^t = -\boldsymbol{C}_n^{t^{-1}} + \boldsymbol{U}^{t^{-1}} \exp(\Delta\zeta \boldsymbol{U}^{t^{-1}} \boldsymbol{A} \boldsymbol{U}^{t^{-1}}) \boldsymbol{U}^{t^{-1}} = \boldsymbol{0} \\ R^\zeta = \|\boldsymbol{Y}^D\| - R = 0 \\ R^\gamma = \|\boldsymbol{E}^t\| - \varepsilon_L = 0 \end{cases} \tag{68}$$

where

$$\boldsymbol{A} = 2\frac{\boldsymbol{Y}^D}{\|\boldsymbol{Y}^D\|}\boldsymbol{C}^t$$

4.3. Consistent tangent matrix

We now linearize the nonlinear equations as it is required for the iterative Newton-Raphson method. For brevity, we report the construction of the tangent matrix only for the case of the saturated phase transformation, corresponding to (66). Linearizing (66), we obtain

$$\begin{cases} \boldsymbol{R}^t + \boldsymbol{R}^t_{,\boldsymbol{U}^t} : d\boldsymbol{U}^t + \boldsymbol{R}^t_{,\Delta\zeta}\, d\Delta\zeta + \boldsymbol{R}^t_{,\gamma}\, d\gamma = \boldsymbol{0} \\ R^\zeta + R^\zeta_{,\boldsymbol{U}^t} : d\boldsymbol{U}^t + R^\zeta_{,\Delta\zeta}\, d\Delta\zeta + R^\zeta_{,\gamma}\, d\gamma = 0 \\ R^\gamma + R^\gamma_{,\boldsymbol{U}^t} : d\boldsymbol{U}^t + R^\gamma_{,\Delta\zeta}\, d\Delta\zeta + R^\gamma_{,\gamma}\, d\gamma = 0 \end{cases} \tag{69}$$

where subscripts following a comma indicate differentiation with respect to that quantity. The derivatives appearing in the above equations are detailed in [36].

Utilizing the linearized form (69), after converting it to matrix form, a system of eight nonlinear scalar equations is obtained that is solved for $d\boldsymbol{U}^t$, $d\Delta\zeta$ and $d\gamma$.

We now address the construction of the tangent tensor consistent with the time-discrete constitutive model. The use of a consistent tensor preserves the quadratic convergence of the Newton–Raphson method for the incremental solution of the global time-discrete problem, as it is done in the framework of a finite element scheme.

The consistent tangent is computed by linearizing the second Piola–Kirchhof tensor, i.e.,

$$d\boldsymbol{S} = \mathbb{D} : d\boldsymbol{E} = \mathbb{D} : \tfrac{1}{2} d\boldsymbol{C} \tag{70}$$

Recalling that $\boldsymbol{S}$ is a function of $\boldsymbol{C}$ and $\boldsymbol{C}^t$, we can write

$$d\boldsymbol{S} = \frac{\partial \boldsymbol{S}}{\partial \boldsymbol{C}} : d\boldsymbol{C} + \frac{\partial \boldsymbol{S}}{\partial \boldsymbol{U}^t} : d\boldsymbol{U}^t \tag{71}$$

Recasting (71) into a matrix form, we obtain

$$[d\boldsymbol{S}] = \left[\frac{\partial \boldsymbol{S}}{\partial \boldsymbol{C}}\right][d\boldsymbol{C}] + \left[\frac{\partial \boldsymbol{S}}{\partial \boldsymbol{U}^t}\right][d\boldsymbol{U}^t] \tag{72}$$

where we have used $[\cdot]$ to denote the matrix form of the tensorial argument.

We now consider Eq. (66) as a function of $\boldsymbol{C}, \boldsymbol{U}^t, \Delta\zeta$ and γ, and then the corresponding linearization gives

$$\begin{cases} \boldsymbol{R}^t_{,\boldsymbol{C}} : d\boldsymbol{C} + \boldsymbol{R}^t_{,\boldsymbol{U}^t} : d\boldsymbol{U}^t + \boldsymbol{R}^t_{,\Delta\zeta}\, d\Delta\zeta + \boldsymbol{R}^t_{,\gamma}\, d\gamma = \boldsymbol{0} \\ R^\zeta_{,\boldsymbol{C}} : d\boldsymbol{C} + R^\zeta_{,\boldsymbol{U}^t} : d\boldsymbol{U}^t + R^\zeta_{,\Delta\zeta}\, d\Delta\zeta + R^\zeta_{,\gamma}\, d\gamma = 0 \\ R^\gamma_{,\boldsymbol{C}} : d\boldsymbol{C} + R^\gamma_{,\boldsymbol{U}^t} : d\boldsymbol{U}^t + R^\gamma_{,\Delta\zeta}\, d\Delta\zeta + R^\gamma_{,\gamma}\, d\gamma = 0 \end{cases} \tag{73}$$

Recasting (73) into a matrix form, we obtain

$$\begin{bmatrix} d\boldsymbol{U}^t \\ d\zeta \\ d\gamma \end{bmatrix} = -\begin{bmatrix} \boldsymbol{R}^t_{,\boldsymbol{U}^t} & \boldsymbol{R}^t_{,\Delta\zeta} & \boldsymbol{R}^t_{,\gamma} \\ R^\zeta_{,\boldsymbol{U}^t} & R^\zeta_{,\Delta\zeta} & R^\zeta_{,\gamma} \\ R^\gamma_{,\boldsymbol{U}^t} & R^\gamma_{,\Delta\zeta} & R^\gamma_{,\gamma} \end{bmatrix}^{-1} \begin{bmatrix} \boldsymbol{R}^t_{,\boldsymbol{C}} \\ R^\zeta_{,\boldsymbol{C}} \\ R^\gamma_{,\boldsymbol{C}} \end{bmatrix} [d\boldsymbol{C}] \tag{74}$$

Now, using (74), we can compute the matrix $[\mathbb{B}]$ such that

$$[d\boldsymbol{U}^t] = [\mathbb{B}][d\boldsymbol{C}] \tag{75}$$

We then substitute (75) into (72) to obtain the consistent tangent matrix as

$$[\mathbb{D}] = 2\left[\frac{\partial \boldsymbol{S}}{\partial \boldsymbol{C}}\right] + 2\left[\frac{\partial \boldsymbol{S}}{\partial \boldsymbol{U}^t}\right][\mathbb{B}] \tag{76}$$

Finally, Table 3 presents the solution algorithm for the proposed improved, fully symmetric, finite-strain constitutive model.

Remark 3. We highlight that in [22,24] and similarly in [20], $\boldsymbol{C}^t$, $\Delta\zeta$ and γ are considered as unknowns in (68), while in this work we assume $\boldsymbol{U}^t$, $\Delta\zeta$ and γ as unknowns in (66) as it has already been done in a similar works [21,34].

Remark 4. Up to now, all relations have been derived in a completely general manner without specifying the form of the Helmholtz free energy ψ^e, apart from the fact that it is an isotropic function of $\boldsymbol{C}^e$. Despite the hyperelastic strain energy function ψ^e can take any well-known form in finite elasticity, for the numerical examples discussed in Section 5 we use the commonly used Saint–Venant Kirchhoff strain energy function:

$$\psi^e = \frac{\lambda}{2}(\operatorname{tr} \boldsymbol{E}^e)^2 + \mu \operatorname{tr} \boldsymbol{E}^{e^2} \tag{77}$$

which yields

$$\alpha_1 = \frac{\lambda}{4}(\overline{\boldsymbol{C}} : \boldsymbol{1} - 3) - \frac{1}{2}\mu, \quad \alpha_2 = \frac{1}{2}\mu, \quad \alpha_3 = 0 \tag{78}$$

where λ and μ are the Lamè constants.

5. Boundary value problems

In this section, we solve four boundary value problems to validate the adopted fully symmetric model as well as the proposed integration algorithm and the solution procedure. A helical spring and a medical stent are simulated at two different temperatures to show the model capability of capturing both pseudo-elasticity and shape-memory effect. We have recently used these boundary value problems [24] as benchmarks to investigate the efficiency and robustness of different integration schemes. Although the results presented here are the same presented in [24], in this work we are interested in comparing the CPU times for both the original asymmetric and the proposed symmetric constitutive models. In all boundary value examples

Table 3
Solution algorithm for the proposed improved finite-strain constitutive model.

1. compute $\boldsymbol{C} = \boldsymbol{F}^T \boldsymbol{F}$
2. set $\boldsymbol{U}^{t^{TR}} = \boldsymbol{U}^t_n$ to compute f^{TR} and trial solution
3. **if** ($f^{TR} < 0$) **then**
   Accept trial solution, i.e., $\boldsymbol{U}^t = \boldsymbol{U}^{t^{TR}}$
   else
   Solve PT1 system.
   if ($\|\boldsymbol{E}^t\|_{PT1} < \varepsilon_L$) **then**
   Accept PT1 solution, i.e., $\boldsymbol{U}^t = (\boldsymbol{U}^t)_{PT1}$
   else
   Solve PT2 system and set $\boldsymbol{U}^t = (\boldsymbol{U}^t)_{PT2}$
   end if
   end if

we use the following material properties:

$E = 51\,700$ MPa, $\nu = 0.3$, $h = 750$ MPa,

$\varepsilon_L = 7.5\%$, $\beta = 5.6$ MPa °C^{-1}

$T_0 = -25$ °C, $R = 140$ MPa, $A_f = 0$ °C, $M_f = -25$ °C

The temperature in the pseudo-elastic simulations is set to 37 °C, while in the shape-memory effect simulations a temperature of −25 °C is adopted.

For all simulations, we use the commercial nonlinear finite element software ABAQUS/Standard, implementing the described algorithm within a user-defined subroutine UMAT. In order to demonstrate the 1D SMA behavior, we first simulate a cube with an edge length of 1 mm under an applied displacement on one face while the opposite face is fixed. The applied displacement is increased from zero to a maximum value of 0.1 mm and subsequently decreased to zero and increased in the opposite direction to a value of 0.1 mm and finally decreased back to zero. Fig. 1 shows the SMA behavior at two different temperatures.

5.1. Helical spring: pseudo-elastic test

A helical spring (with a wire diameter of 4 mm, a spring external diameter of 24 mm, a pitch size of 12 mm and with two coils and an initial length of 28 mm) is simulated using 9453 quadratic tetrahedron (C3D10) elements and 15 764 nodes. An axial force of 1525 N is applied to one end while the other end is fully clamped. The force is increased from zero to its maximum value and unloaded back to zero. Fig. 2 shows the spring initial geometry, the adopted mesh and the deformed shape under the maximum force. After unloading, the spring recovers the original shape as it is expected in the pseudo-elastic regime. Fig. 3 (top) shows the force-displacement diagram. It is observed that the spring shape is fully recovered after load removal.

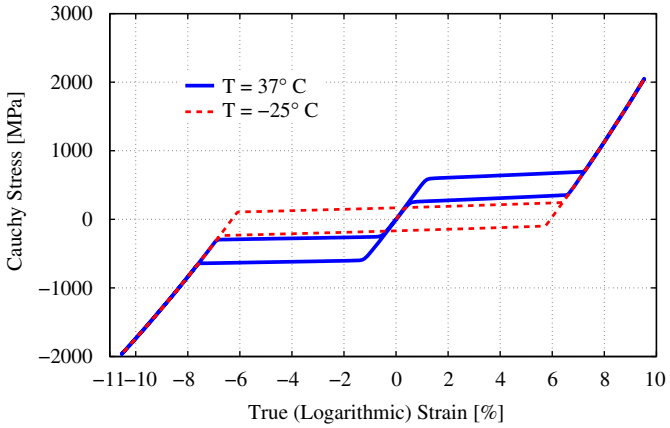

Fig. 1. 1D SMA behavior: pseudo-elasticity at $T = 37$ °C and shape-memory effect at $T = -25$ °C.

5.2. Helical spring: shape-memory effect test

We also simulate the same spring of Section 5.1 in the case of shape-memory effect. An axial force of 427 N is applied at $T = -25$ °C (Fig. 4, top) and, after unloading, the spring does not recover its initial shape (Fig. 4, bottom). After heating, up to a temperature of 10 ° C, the spring recovers its original shape. Fig. 3 (right) shows the force-displacement-temperature behavior. According to Fig. 3 (bottom), heating the spring leads to full recovery of the original shape at $T = A_f$ (0 °C) and subsequent heating does not change its shape anymore.

5.3. Crimping of a medical stent: pseudo-elastic test

In this example, the crimping of a pseudo-elastic medical stent is simulated. To this end a medical stent with 0.216 mm thickness and an initial outer diameter of 6.3 mm (Fig. 5, top-left) is crimped to an outer diameter of 1.5 mm. Utilizing the ABAQUS/Standard contact module, the contact between the catheter and the stent is considered in the simulation. A radial displacement is applied to

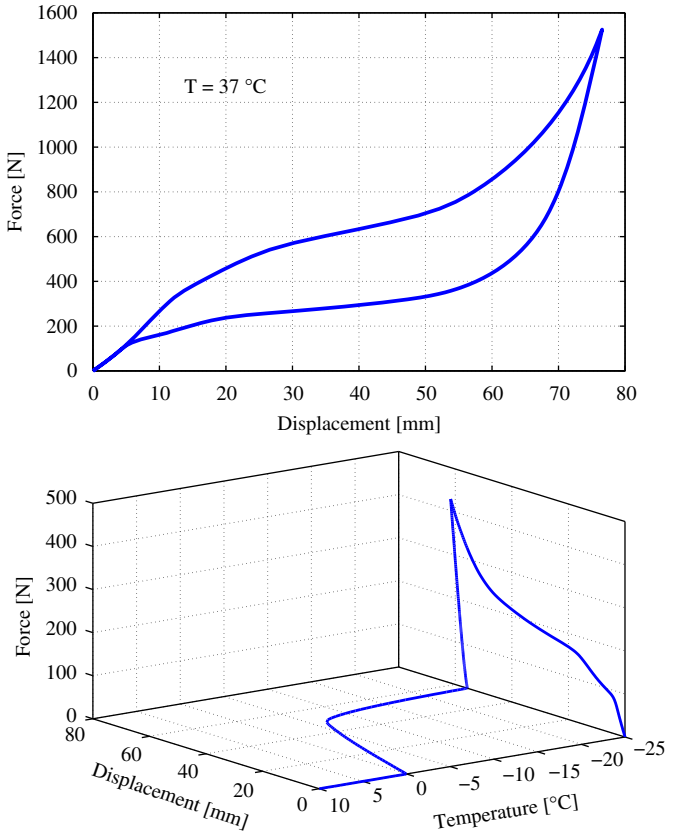

Fig. 3. Force-displacement diagram for the SMA spring: pseudo-elasticity (top) and shape-memory effect (bottom).

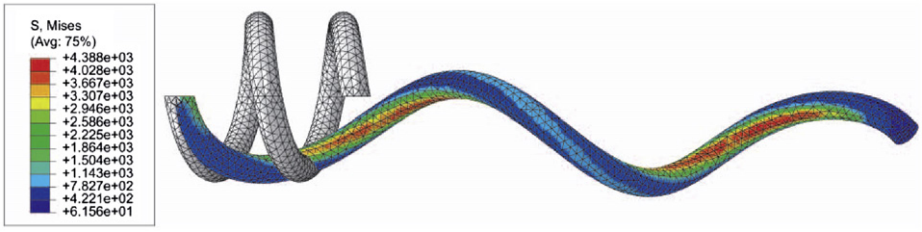

Fig. 2. Pseudo-elastic spring: comparison of initial geometry and deformed configuration.

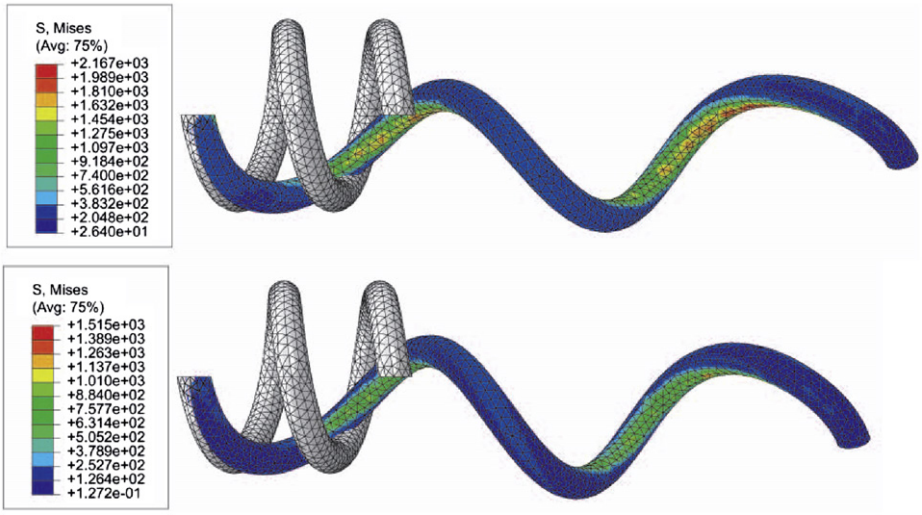

Fig. 4. Shape-memory effect in the simulated spring: deformed shape under maximum load (top) and after unloading (bottom).

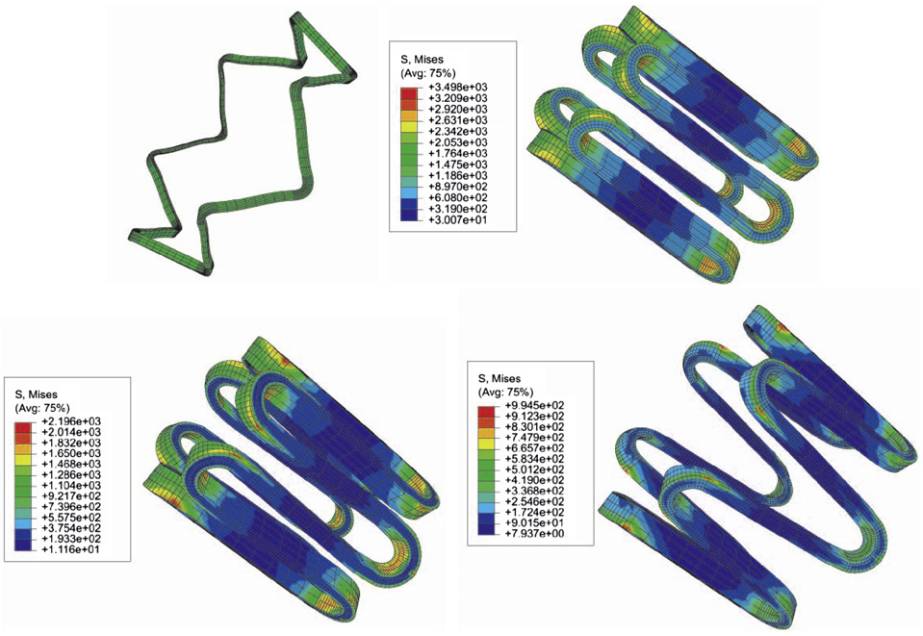

Fig. 5. Stent crimping: initial geometry (top-left), crimped shape in PE case (top-right), crimped shape in SME case (bottom-left) and deformed shape in SME case after uncrimping (bottom-right).

the catheter and is then released to reach the initial diameter. In this process, the stent recovers its original shape after unloading. Fig. 5 (top-right) shows the stent deformed shape when crimped.

5.4. Crimping of a medical stent: shape-memory effect test

In this example, the same stent is crimped at a temperature of $-25\,^{\circ}\mathrm{C}$ as it is shown in Fig. 5 (bottom-left). Due to the low temperature, while the catheter is expanded, the stent remains in a deformed state as shown in Fig. 5 (bottom-right). The initial shape is, however, recovered after heating.

5.5. Comparison of CPU times

We now compare the CPU times for three cases, i.e., original unsymmetric model in which $\boldsymbol{C}^t$ is considered as unknown [22,24], the original unsymmetric model in which $\boldsymbol{U}^t$ is considered as unknown and the proposed symmetric model in which $\boldsymbol{U}^t$ is considered as unknown. We denote them as *original-C*, *original-U* and *improved*, respectively, in the following.

We remark that we normalize all CPU times with respect to those for the case *original-C* [22,24]. Moreover, the models have been programmed in a consistent manner, so that reliable comparisons concerning the speed of computation could be obtained.

The simulation CPU times are reported in Table 4. From such results we may conclude that using $\boldsymbol{U}^t$ instead of $\boldsymbol{C}^t$, decreases the CPU time of approximately one third compared with that adopted in [22,24].

Moreover, comparing *original-U* and *improved* CPU times, we observe a slightly increased efficiency for the proposed symmetric model.

We finally, conclude that using the proposed symmetric constitutive model and solution algorithm can improve the

Table 4
Normalized CPU time comparison.

	Spring (PE)	Spring (SME)	Stent (PE)	Stent (SME)
original-C	1.00	1.00	1.00	1.00
original-U	0.68	0.72	0.65	0.72
improved	0.64	0.69	0.63	0.73

numerical efficiency in the order of one third when compared with the previously adopted ones in [22,24].

6. Conclusions

In this paper, we investigate a 3D finite-strain constitutive model which is fully expressed in terms of symmetric tensors. The derivation is based on a multiplicative decomposition of the deformation gradient into elastic and transformation parts and satisfying the second law of thermodynamics in Clausius–Duhem inequality form. Based on an exponential mapping, we propose a time-discrete form of the evolution equation which conserves the volume during inelastic deformations. Implementing the proposed model within a user-defined subroutine (UMAT) in the commercial nonlinear finite element software ABAQUS, we solve different boundary value problems. Comparing the CPU times, we show the efficiency of the proposed constitutive model as well as the solution algorithm, implying a solution time reduction of around one third (33%) with respect to the original asymmetric model. Moreover, we show that the improved efficiency is mostly due to the simplification in computing fourth-order tensors appearing in the linearization procedure.

Acknowledgements

J. Arghavani has been partially supported by Iranian Ministry of Science, Research and Technology, and partially by Dipartimento di Meccanica Strutturale, Università degli Studi di Pavia.

F. Auricchio and A. Reali have been partially supported by the Cariplo Foundation through the Project no. 2009.2822; by the Ministero dell'Istruzione, dell'Università e della Ricerca through the Project no. 2008MRKXLX; and by the European Research Council through the Starting Independent Research Grant "BioSMA: Mathematics for Shape Memory Technologies in Biomechanics".

References

[1] K. Otsuka, C.M. Wayman, Shape Memory Materials, Cambridge University Press, Cambridge, 1998.
[2] T.W. Duerig, K.N. Melton, D. Stoekel, C.M. Wayman, Engineering Aspects of Shape Memory Alloys, Butterworth-Heinemann, London, 1990.
[3] T. Duerig, A. Pelton, D. Stckel, An overview of nitinol medical applications, Materials Science and Engineering A 273–275 (1999) 149–160.
[4] K. Kuribayashi, K. Tsuchiya, Z. You, D. Tomus, M. Umemoto, T. Ito, M. Sasaki, Self-deployable origami stent grafts as a biomedical application of Ni-rich TiNi shape memory alloy foil, Materials Science and Engineering A 419 (2006) 131–137.
[5] H. Funakubo, Shape Memory Alloys, Gordon and Breach Science Publishers, New York, 1987.
[6] B. Raniecki, C. Lexcellent, Thermodynamics of isotropic pseudoelasticity in shape memory alloys, European Journal of Mechanics—A/Solids 17 (1998) 185–205.
[7] M. Panico, L. Brinson, A three-dimensional phenomenological model for martensite reorientation in shape memory alloys, Journal of the Mechanics and Physics of Solids 55 (2007) 2491–2511.
[8] A.C. Souza, E.N. Mamiya, N. Zouain, Three-dimensional model for solids undergoing stress-induced phase transformations, European Journal of Mechanics—A/Solids 17 (1998) 789–806.
[9] D. Helm, P. Haupt, Shape memory behaviour: modelling within continuum thermomechanics, International Journal of Solids and Structures 40 (2003) 827–849.
[10] C. Bouvet, S. Calloch, C. Lexcellent, A phenomenological model for pseudoelasticity of shape memory alloys under multiaxial proportional and nonproportional loadings, European Journal of Mechanics—A/Solids 23 (2004) 37–61.
[11] P. Popov, D.C. Lagoudas, A 3-D constitutive model for shape memory alloys incorporating pseudoelasticity and detwinning of self-accommodated martensite, International Journal of Plasticity 23 (2007) 1679–1720.
[12] F. Thiebaud, C. Lexcellent, M. Collet, E. Foltete, Implementation of a model taking into account the asymmetry between tension and compression, the temperature effects in a finite element code for shape memory alloys structures calculations, Computational Materials Science 41 (2007) 208–221.
[13] Z. Moumni, W. Zaki, Q.S. Nguyen, Theoretical and numerical modeling of solid–solid phase change: application to the description of the thermomechanical behavior of shape memory alloys, International Journal of Plasticity 24 (2008) 614–645.
[14] J. Arghavani, F. Auricchio, R. Naghdabadi, A. Reali, S. Sohrabpour, A 3-D phenomenological constitutive model for shape memory alloys under multiaxial loadings, International Journal of Plasticity 26 (2010) 976–991.
[15] R. Mahnken, S. Wilmanns, Simulation of asymmetric effects for shape memory alloys by decomposition of transformation strains, Computational Materials Science 42 (2008) 295–305.
[16] Y. Wang, Z. Yue, J. Wang, Experimental and numerical study of the superelastic behaviour on niti thin-walled tube under biaxial loading, Computational Materials Science 40 (2007) 246–254.
[17] F. Auricchio, R.L. Taylor, Shape-memory alloys: modelling and numerical simulations of the finite-strain superelastic behavior, Computer Methods in Applied Mechanics and Engineering 143 (1997) 175–194.
[18] F. Auricchio, A robust integration-algorithm for a finite-strain shape-memory-alloy superelastic model, International Journal of Plasticity 17 (2001) 971–990.
[19] A. Ziolkowski, Three-dimensional phenomenological thermodynamic model of pseudoelasticity of shape memory alloys at finite strains, Continuum Mechanics and Thermodynamics 19 (2007) 379–398.
[20] S. Reese, D. Christ, Finite deformation pseudo-elasticity of shape memory alloys—constitutive modelling and finite element implementation, International Journal of Plasticity 24 (2008) 455–482.
[21] D. Christ, S. Reese, A finite element model for shape memory alloys considering thermomechanical couplings at large strains, International Journal of Solids and Structures 46 (2009) 3694–3709.
[22] V. Evangelista, S. Marfia, E. Sacco, A 3D SMA constitutive model in the framework of finite strain, International Journal for Numerical Methods in Engineering 81 (6) (2010) 761–785.
[23] J. Arghavani, F. Auricchio, R. Naghdabadi, A. Reali, S. Sohrabpour, A 3D finite strain phenomenological constitutive model for shape memory alloys considering martensite reorientation, Continuum Mechanics and Thermodynamics 22 (2010) 345–362, doi:10.1007/s00161-010-0155-8.
[24] J. Arghavani, F. Auricchio, R. Naghdabadi, A. Reali, On the robustness and efficiency of integration algorithms for a 3D finite strain phenomenological SMA constitutive model, International Journal for Numerical Methods in Engineering, accepted for publication, doi:10.1002/nme.2964.
[25] P. Thamburaja, A finite-deformation-based phenomenological theory for shape-memory alloys, International Journal of Plasticity 26 (8) (2010) 1195–1219.
[26] C. Muller, O. Bruhns, A thermodynamic finite-strain model for pseudoelastic shape memory alloys, International Journal of Plasticity 22 (2006) 1658–1682.
[27] F. Auricchio, L. Petrini, Improvements and algorithmical considerations on a recent three-dimensional model describing stress-induced solid phase transformations, International Journal for Numerical Methods in Engineering 55 (2002) 1255–1284.
[28] F. Auricchio, L. Petrini, A three-dimensional model describing stress-temperature induced solid phase transformations: thermomechanical coupling and hybrid composite applications, International Journal for Numerical Methods in Engineering 61 (2004) 716–737.
[29] F. Auricchio, L. Petrini, A three-dimensional model describing stress-temperature induced solid phase transformations: solution algorithm and boundary value problems, International Journal for Numerical Methods in Engineering 61 (2004) 807–836.
[30] V.A. Lubarda, Elastoplasticity Theory, CRC Press, 2001.
[31] P. Haupt, Continuum Mechanics and Theory of Materials, Springer Publication House, 2002.
[32] A.L. Eterovic, K.-J. Bathe, A hyperelastic-based large strain elasto-plastic constitutive formulation with combined isotropic-kinematic hardening using the logarithmic stress and strain measures, International Journal for Numerical Methods in Engineering 30 (1990) 1099–1114.
[33] C. Miehe, Exponential map algorithm for stress updates in anisotropic multiplicative elastoplasticity for single crystals, International Journal for Numerical Methods in Engineering 39 (1996) 3367–3390.
[34] I.N. Vladimirov, M.P. Pietryga, S. Reese, On the modelling of non-linear kinematic hardening at finite strains with application to springback—comparison of time integration algorithms, International Journal for Numerical Methods in Engineering 75 (2008) 1–28.
[35] I.N. Vladimirov, M.P. Pietryga, S. Reese, Anisotropic finite elastoplasticity with nonlinear kinematic and isotropic hardening and application to sheet metal forming, International Journal of Plasticity 26 (5) (2010) 659–687.
[36] J. Arghavani, Thermomechanical behavior of shape memory alloys under nonproportional loading: constitutive modelling and numerical inplementation in small and finite strains, Ph.D. Thesis, Sharif University of Technology, Iran, 2010.